Medical Engineering and Physics 47 (2017) 38–46

Contents lists available at ScienceDirect

Medical Engineering and Physics

journal homepage: www.elsevier.com/locate/medengphy

Large eddy simulations of blood dynamics in abdominal aortic aneurysms

Christian Vergara[a,*], Davide Le Van[a], Maurizio Quadrio[b], Luca Formaggia[a], Maurizio Domanin[c,d]

[a] MOX, Dipartimento di Matematica, Politecnico di Milano, Italy
[b] Dipartimento di Scienze e Tecnologie Aerospaziali, Politecnico di Milano, Italy
[c] Operative Unit of Vascular Surgery, Fondazione I.R.C.C.S. Ca' Granda Ospedale Maggiore Policlinico di Milano, Italy
[d] Department of Clinical Sciences and Community, Universitá di Milano, Italy

ARTICLE INFO

Article history:
Received 20 February 2017
Revised 2 June 2017
Accepted 14 June 2017

Keywords:
Abdominal aortic aneurysm
Large eddy simulation
Ensemble-average
Transition to turbulence

ABSTRACT

We study the effects of transition to turbulence in abdominal aortic aneurysms (AAA). The presence of transitional effects in such districts is related to the heart pulsatility and the sudden change of diameter of the vessels, and has been recorded by means of clinical measures as well as of computational studies. Here we propose, for the first time, the use of a large eddy simulation (LES) model to accurately describe transition to turbulence in realistic scenarios of AAA obtained from radiological images. To this aim, we post-process the obtained numerical solutions to assess significant quantities, such as the ensemble-averaged velocity and wall shear stress, the standard deviation of the fluctuating velocity field, and vortical structures educed via the so-called Q-criterion. The results demonstrate the suitability of the considered LES model and show the presence of significant transitional effects around the impingement region during the mid-deceleration phase.

1. Introduction

Dynamics of blood plays a major role in the development of abdominal aortic aneurysms (AAA), an enlargement of the abdominal aorta whose rupture could lead to fatal events [1]. In particular, specific wall shear stress (WSS) conditions regulate the production of nitric oxide [2], which is known to cause the loss of elastin which is at the root of aneurysm formation and growth; cause the activation of blood platelets [3], playing a central role in thrombus formation; and are responsible for anisotropic displacements of the aneurysmatic sac [4].

In this context, the possibility for the flow regime to be transitional or turbulent owing to the enlargement of the lumen and to pulsatility [5,6] has a strong impact on WSS and thus on the above-mentioned relationships. In particular, turbulence effects are responsible for an increased platelets activation [7] and damage of the blood cell [8], and provide additional mechanical stresses that may lead to further AAA dilatation [9]. Although not determined mainly by WSS, also the rupture process may be influenced by turbulence in the aneurysm, since the corresponding arterial wall vibration may damage the structural components of the wall [10].

For these reasons, the inclusion of turbulence effects (via turbulence models, or the use of very fine meshes) is mandatory for a computational study of blood dynamics in AAA and for an accurate description of the aneurysm evolution [9–11]. One major issue relies on the qualification and quantification of turbulence, since its very definition is in general problematic, and particularly so in hemodynamics. Indeed, in this context turbulence does not fully develop since the acceleration at the beginning of a new heartbeat laminarizes the flow which thus can only experience a transitional behavior [8]. This is a common fact in vascular hemodynamics, for example in stenotic carotids [12–15] and cerebral aneurysms [16,17]. Often, some authors describe with the term "turbulent" blood flows which are simply unsteady and/or vortical. Only few computational studies have introduced suitable statistically-based quantities to assess turbulence effects in AAA [10,11].

In this work, we consider large eddy simulations (LES) for the study of transition to turbulence effects in AAA. In particular, we apply the eddy-viscosity σ–model [18] to three patient-specific geometries. To assess turbulence effects, we study the standard deviation of the velocity field, the ratio between eddy and molecular viscosities, and the fluctuations of the kinetic energy. Our results show the suitability of LES models in hemodynamics and the

* Corresponding author.
E-mail addresses: christian.vergara@polimi.it (C. Vergara), davide.le@mail.polimi.it (D. Le Van), maurizio.quadrio@polimi.it (M. Quadrio), luca.formaggia@polimi.it (L. Formaggia), maurizio.domanin@unimi.it (M. Domanin).

http://dx.doi.org/10.1016/j.medengphy.2017.06.030
1350-4533/

presence of a significant amount of transitional effects localized close to the jet impingement region during the deceleration phase.

2. Materials and methods

2.1. Geometric data

Three patients (denoted P1, P2, and P3 in what follows) who underwent 4D-CT as preoperative evaluation of an AAA were selected for inclusion in the present study, which was approved by the ethical review board of the hospital where the patients were treated. The patients gave informed consent. The radiological acquisitions were performed with a Somatom Definition Dual Source CT (Siemens, Erlangen, Germany), before and after contrast media administration with retrospectively electrocardiographic (ECG) gated spiral acquisition. Non-ionic contrast media (Iomeron, Bracco, Milan, Italy) was used with a concentration of 400 mg/I mg, 1.5 cc pro kg, and an injection speed of 3 cc/s. The temporal resolution was 85 ms, and the total effective dose according to the applied protocol was 34 mSv per acquisition and per patient.

The 3D geometric reconstructions were performed by means of the Vascular Modeling Toolkit, VMTK [19]. The 3D surface model of the lumen surface of the abdominal aorta was reconstructed using a gradient-driven level set technique. Then, the surface models of the three geometries were turned into volumetric meshes of linear tetrahedra, with three thin layers close to the wall. In particular, the meshes were formed by 275 k and 110 k tetrahedra for P1, 115k tetraedra for P2, and 120 k tetraedra for P3. These values correspond to a characteristic space discretization parameter $h = 0.08$ cm and $h = 0.11$ cm for P1, and $h = 0.13$ cm for P2 and P3.

2.2. Numerical methods

Blood is modelled as a constant density, Newtonian and homogeneous fluid, a well accepted hypothesis for medium and large vessels [20].

LES models are based on the decomposition of the fluid unknowns in resolved and unresolved quantities, $[\overline{\boldsymbol{u}}, \overline{p}]$ and $[\boldsymbol{u}', p']$, respectively, so that $\boldsymbol{u} = \overline{\boldsymbol{u}} + \boldsymbol{u}'$ and $p = \overline{p} + p'$ [21]. The resolved quantities are referred to as filtered. To derive a set of equations for $\overline{\boldsymbol{u}}$ and $\overline{p}$, a formal filtering procedure is applied to the Navier–Stokes equations. Defining the subgrid-scale tensor $\boldsymbol{\tau} = \overline{\boldsymbol{u} \otimes \boldsymbol{u}} - \overline{\boldsymbol{u}} \otimes \overline{\boldsymbol{u}}$, which models the effect of the unresolved scales on the resolved ones [22,23], we consider the following filtered Navier–Stokes problem (normalized over the fluid density):

Find the velocity $\overline{\boldsymbol{u}}(t, \boldsymbol{x})$ and the pressure $\overline{p}(t, \boldsymbol{x})$ such that

$$\frac{\partial \overline{\boldsymbol{u}}}{\partial t} - \nu \nabla \cdot \boldsymbol{S}(\overline{\boldsymbol{u}}) + \nabla \cdot (\overline{\boldsymbol{u}} \otimes \overline{\boldsymbol{u}}) + \nabla \overline{p} + \nabla \cdot \boldsymbol{\tau}^d(\overline{\boldsymbol{u}}) = \boldsymbol{0} \quad t \in (0, MT],\ \boldsymbol{x} \in \Omega, \tag{1a}$$

$$\nabla \cdot \overline{\boldsymbol{u}} = 0 \qquad t \in (0, MT],\ \boldsymbol{x} \in \Omega, \tag{1b}$$

$$\overline{\boldsymbol{u}} = \boldsymbol{g} \qquad t \in (0, MT],\ \boldsymbol{x} \in \Gamma_{in}, \tag{1c}$$

$$-\overline{p}\boldsymbol{n} + \nu \boldsymbol{S}(\overline{\boldsymbol{u}})\boldsymbol{n} - \boldsymbol{\tau}^d(\overline{\boldsymbol{u}})\boldsymbol{n} = \boldsymbol{0} \qquad t \in (0, MT],\ \boldsymbol{x} \in \Gamma_{out}, \tag{1d}$$

with zero initial boundary condition for the velocity, and where M is the number of heartbeats, T the period of a heartbeat, $(\boldsymbol{u} \otimes \boldsymbol{u})_{ij} = u_i u_j$, $\boldsymbol{S}(\boldsymbol{u}) = \nabla \boldsymbol{u} + (\nabla \boldsymbol{u})^T$, Γ_{in} is the inlet, Γ_{out} the two outlets given by the iliac segments, ν is the kinematic viscosity, and $\boldsymbol{g}(t, \boldsymbol{x})$ is a given boundary data. In particular, at the inlet Γ_{in} we impose for all the three patients the representative time variation of the flow rate $Q(t)$ reported in Fig. 1. The systolic Reynolds numbers at the inlet for the three cases are 1277, 1220, 1186, respectively. Here, the flow rate is defined as

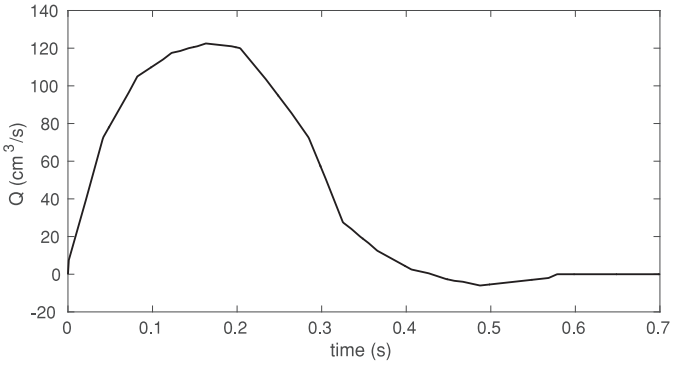

Fig. 1. Flow waveform prescribed at the inlet.

$$Q = \int_{\Gamma_{in}} \overline{\boldsymbol{u}} \cdot \boldsymbol{n}\, d\sigma. \tag{2}$$

This is a defective boundary condition, since at each time step we are prescribing only a scalar quantity over the whole Γ_{in}. In order to fill this gap, we make the assumption of a parabolic velocity profile along the normal direction, yielding the Dirichlet condition (1c), $\boldsymbol{g}$ being the unique function with a parabolic profile in the normal direction and vanishing in the tangential ones, with flow rate equal to $Q(t)$. No perturbation is prescribed, so that the flow is assumed to be laminar at the inlet boundary. This will allow us to capture transitional effects arising as a consequence of geometry and pulsatility solely. The tensor $\boldsymbol{\tau}^d = \boldsymbol{\tau} - \frac{1}{3}\sum_k \tau_{kk}\boldsymbol{I}$ in (1) is the deviatoric part of the subgrid-scale tensor $\boldsymbol{\tau}$. The latter is suitably modeled as a function of the filtered quantities $\overline{\boldsymbol{u}}$, hence Eq. (1) have only $(\overline{\boldsymbol{u}}, \overline{p})$ as dependent variables. Usually, the effect of the subgrid-scale on the resolved scales is modeled in analogy with the kinetic theory of gases, by introducing a subgrid-scale viscosity ν_{sgs} and by modeling the deviatoric part of the subgrid-scale tensor as follows:

$$\boldsymbol{\tau}^d(\overline{\boldsymbol{u}}) = -2\nu_{sgs}(\overline{\boldsymbol{u}})\boldsymbol{S}(\overline{\boldsymbol{u}}).$$

The eddy viscosity model considered in this work is the σ−model, introduced in [18]. This is based on the introduction of the singular values $\sigma_1(t, \boldsymbol{x}) \geq \sigma_2(t, \boldsymbol{x}) \geq \sigma_3(t, \boldsymbol{x}) \geq 0$ of $\nabla \overline{\boldsymbol{u}}$, and on defining the subgrid-scale viscosity as follows:

$$\nu_{sgs} = C\overline{\Delta}^2 \frac{\sigma_3(\sigma_1 - \sigma_2)(\sigma_2 - \sigma_3)}{\sigma_1^2}, \tag{3}$$

where C is a suitable constant and $\overline{\Delta}$ the filter width. In our simulation we set $C = 1.5$ [18,24]. For the grid filter we considered an *implicit* procedure [25], where the filter width $\overline{\Delta}$ represents the size of a mesh that is not able to capture all the scales [23]. This empirical choice is the most widely used nowadays.

As for the time discretization, we use a semi-implicit approach to linearize the momentum Eq. (1a), used in combination with a BDF2 scheme [26]. In particular, the convective field and the subgrid-scale viscosity have been evaluated by means of a second order extrapolation [24]. This treatment yields a CFL-like limitation on the time step Δt ($\Delta t \lesssim h$ [27]). For the space discretization we use Finite Elements with a SUPG stabilization term added to control numerical instabilities due to the large convective term [28]. We used $P2 - P2$ Finite Elements, that is piecewise quadratic polynomials for the approximation of the pressure and each velocity component. A Pressure Stabilized Petrov–Galerkin (PSPG) formulation [28] was used to ensure the non-singularity of the

corresponding matrix. For the description of the complete discretized-in-time problem, we refer the reader elsewhere [24].

We use the following data: physical viscosity $\nu = 0.033\,\mathrm{cm}^2/\mathrm{s}$, time discretization parameter $\Delta t = 0.001\,\mathrm{s}$, number of heartbeats $M = 6$ and heartbeat period $T = 0.7\,\mathrm{s}$.

All numerical results have been obtained using the parallel Finite Element library LIFEV (www.lifev.org).

2.3. Quantities of interest

To describe the blood dynamics and in particular transitional effects in the three AAA geometries, we introduce the following operators and post-processed quantities:

- *Ensemble-average*. Given a quantity $S(t, \boldsymbol{x})$, we define its ensemble-average as

$$< S(t,\boldsymbol{x}) >= \frac{1}{M}\sum_{j=1}^{M} S(t+(j-1)T,\boldsymbol{x}), \quad t \in (0,T].$$

  This allows us to remove from the field of interest the random, zero-time-mean fluctuations due to the transitional effects appearing at each heartbeat. In this study, we consider the ensemble-average velocity magnitude $< U >$ and wall shear stress $< WSS >$, where

$$U(t,\boldsymbol{x}) = \|\overline{\boldsymbol{u}}(t,\boldsymbol{x})\|_{\mathbb{R}^3} \quad WSS(t,\boldsymbol{x}) = \nu\sqrt{\sum_{j=1}^{2}\left(\nabla\overline{\boldsymbol{u}}\,\boldsymbol{n})\cdot\boldsymbol{\tau}^{(j)}\right)^2}, \quad t \in (0,MT],$$

  the latter quantity is computed on the lateral surface, $\boldsymbol{n}$ is the outward unit vector, and $\boldsymbol{\tau}^{(j)}$, $j = 1, 2$, the tangential unit vectors;
- *Standard deviation of the fluctuations of the velocity magnitude*. This is defined as

$$SD(t,\boldsymbol{x}) = \sqrt{\frac{1}{M}\sum_{j=1}^{M}(U(t+(j-1)T,\boldsymbol{x}) - < U(t,\boldsymbol{x}) >)^2}, \ t \in (0,T].$$

  This allows us to quantify and localize the velocity fluctuations among the heartbeats
- *Q-criterion*. The scalar field Q is defined as

$$Q(t,\boldsymbol{x}) = -\frac{1}{2}\left(\sum_{i,j} S_{ij}^2(t,\boldsymbol{x}) - \Omega_{ij}^2(t,\boldsymbol{x})\right), \quad t \in (0,MT],$$

  where $\boldsymbol{\Omega} = \nabla\overline{\boldsymbol{u}} - (\nabla\overline{\boldsymbol{u}})^T$ [14,29]. Positive values of Q indicate locations where rotations dominates over strain and shear. This allows us to identify regions where vortical structures are present
- *Global Turbulent Kinetic Energy*. It is defined as the space integral of the Turbulent Kinetic Energy ($TKE(t, \boldsymbol{x})$) [11]:

$$k(t) = \frac{1}{2}\int_\Omega \frac{1}{M}\sum_{j=1}^{M}\Big((\overline{u}_x(t+(j-1)T,\boldsymbol{x}) - < u_x(t,\boldsymbol{x}) >)^2 + (\overline{u}_y(t+(j-1)T,\boldsymbol{x}) - < u_y(t,\boldsymbol{x}) >)^2 + (\overline{u}_z(t+(j-1)T,\boldsymbol{x}) - < u_z(t,\boldsymbol{x}) >)^2\Big)d\boldsymbol{x}, \quad t \in (0,T].$$

  TKE is representative of the cycle-to-cycle variation of the velocity field and its spatial average $k(t)$ allows us to identify the temporal instants within the heartbeat where fluctuations in the whole AAA are more pronounced. Moreover, the average and maximum value of $k(t)$, here indicated as k_{mean} and k_{max}, respectively, are proposed in this study as synthetic indices to quantify the amount of variability of the velocity field in the aneurysmatic sac and thus the possible presence of transitional effects.

3. Results

3.1. Assessment of the computational meshes

The goal of LES simulations is to accurately describe turbulent flows on a coarser mesh than the one needed to perform a Direct Numerical Simulation (DNS), where all the significant scale of motions would need to be resolved. A suitable mesh for a LES model should be neither too fine, in order to be a valid alternative to DNS, nor too coarse, such that the assumptions underlying the LES model remain valid. To this aim, in this first set of simulations, we compare the results obtained for patient P1 with two meshes in order to estimate the number of tetrahedra of a reasonable mesh.

Referring to the results reported in Fig. 2, we first observe that, as expected, blood flow is characterized by a jet that impinges on the distal part of the aneurysmatic sac (see figures at the top, where the ensemble-averaged velocity magnitude $< U >$ over the 6 heartbeats has been plotted). Secondly, we observe an excellent qualitative agreement between $< U >$ computed in the two meshes. This suggests that the coarser mesh is suitable for our purposes. This is also confirmed by the ratio between the subgrid-scale and molecular viscosities, reported in Fig. 2, bottom. These figures clearly indicate the presence of transitional effects in the aneurismatic sac, in particular at the mid-deceleration and early diastolic phases. The subgrid-scale viscosity reaches values up to five times the molecular one in the coarsest mesh and up to 3 times in the finest one. This means that the contribution of the subgrid-scale modeling is, as expected, greater for the coarsest mesh in order to account for the higher frequency cutoff introduced in this case by the implicit filter. At the same time, the numerical errors introduced by the coarsest mesh are still small enough not to compromise accuracy, since the results are in accordance with the finest mesh. For all these reasons, in what follows we consider for P2 and P3 meshes of the same level of refinement as the coarsest mesh used for P1.

3.2. Description of transitional effects

In Fig. 3 we report for P2 and P3 the same quantities plotted in Fig. 2 for P1, i.e. the ensemble-averaged velocity magnitude over 6 heartbeats and the ratio between the subgrid-scale and molecular viscosities. From these figures we observe again the jet impingement in the distal region of the aneurysmatic sac of P2. Instead, for P3 the non-axiality of the tract of the aorta just above the sac forces the jet to impinge on the proximal part of the sac. Moreover, we observe that, as for P1, for both P2 and P3 the LES model is active, in particular during the mid-deceleration and early diastolic phases, with the subgrid-scale viscosity reaching values up to five times greater than those of the molecular viscosity.

In Fig. 4, left, we report for all three cases the values of the standard deviation of the velocity magnitude over 6 heartbeats at the same three time instants as before. These plots show high values of the standard deviation for all the three cases at the early diastole and also at the mid-deceleration phase for P1 and P3. These values are of the same order of magnitude of the velocity itself (look at Figs. 2 and 3). In the same figure, on the right, we plot the vortical structures identified by means of the Q-criterion. We have the formation of a vortex ring at the systolic peak which impinges the aneurysmatic sac at the mid-deceleration phase and, after the breakage, partially exits through the iliac outlets.

In Fig. 5 we report the time evolution of the global Turbulent Kinetic Energy over 6 heartbeats for the three patients.

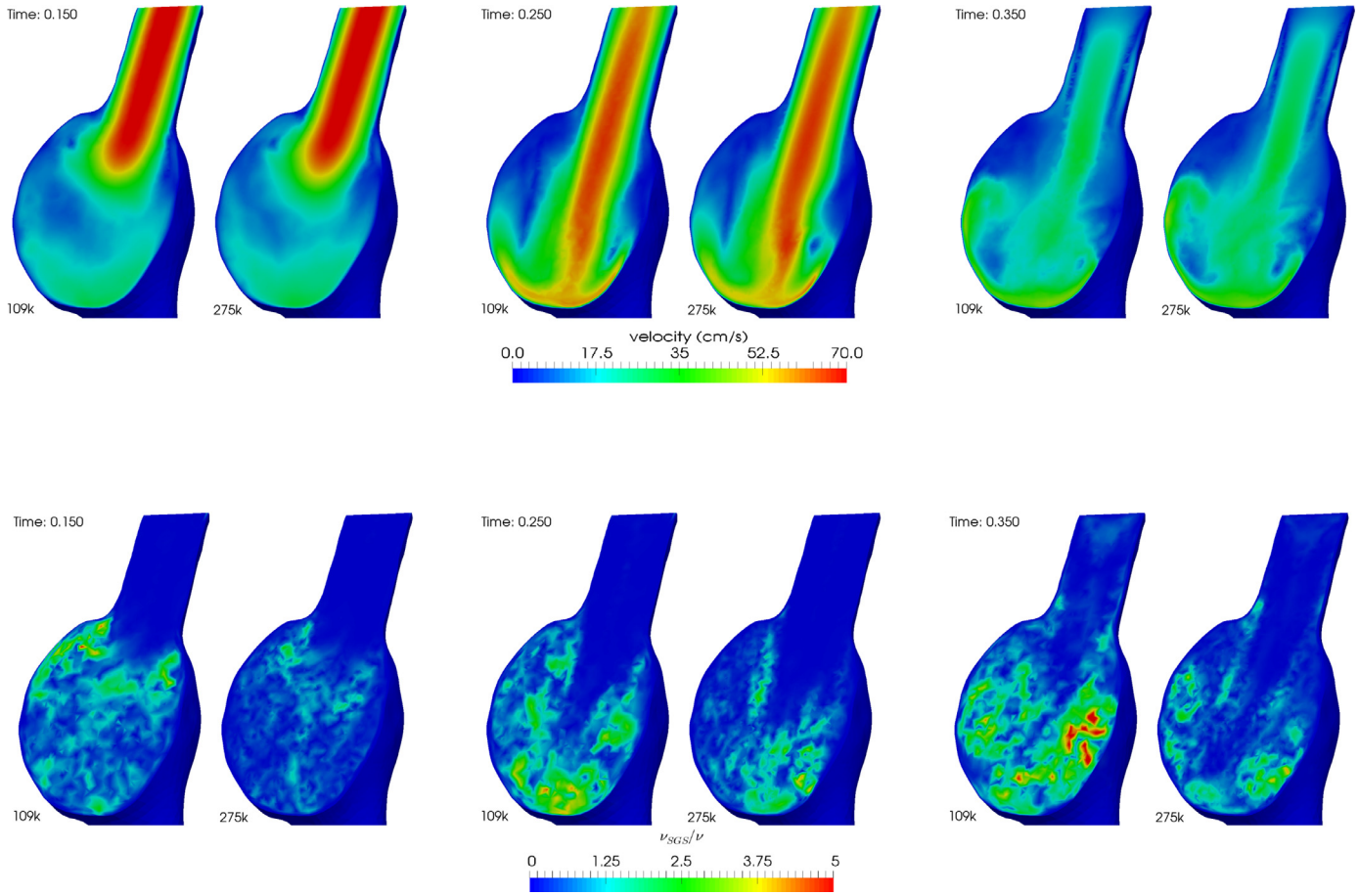

Fig. 2. Top: Ensemble-averaged velocity magnitude over 6 heartbeats; Bottom: Ratio between the subgrid-scale and molecular viscosities. In each figure, we report on the left the results obtained with the coarse mesh and on the right those obtained with the fine mesh. Three time instants are reported: Systolic peak instant $t = 0.15\,s$ (left); Mid-deceleration $t = 0.25\,s$ (middle); Early diastole $t = 0.35\,s$ (right).

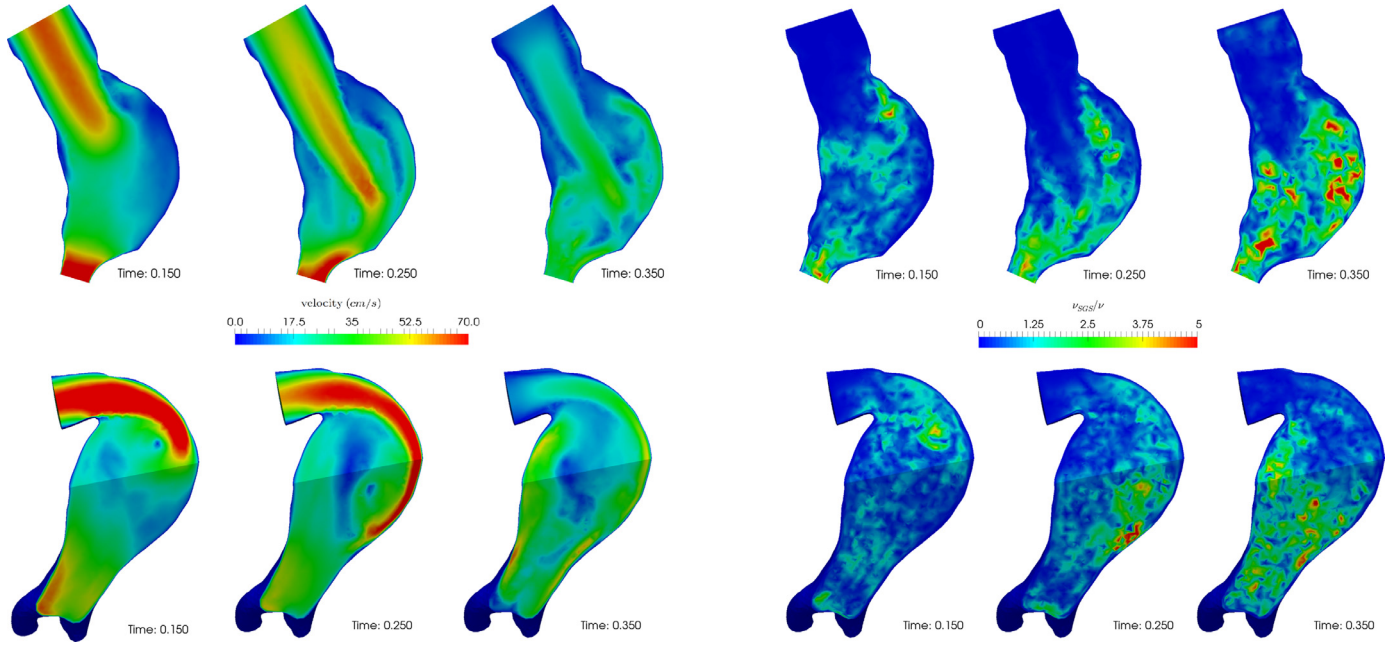

Fig. 3. Left: Ensemble-averaged velocity magnitude over 6 heartbeats; Right: Ratio between the subgrid-scale and molecular viscosities. Top: Results for P2; Bottom: Results for P3. Three time instants are reported: Systolic peak instant $t = 0.15\,s$ (left); Mid-deceleration $t = 0.25\,s$ (middle); Early diastole $t = 0.35\,s$ (right).

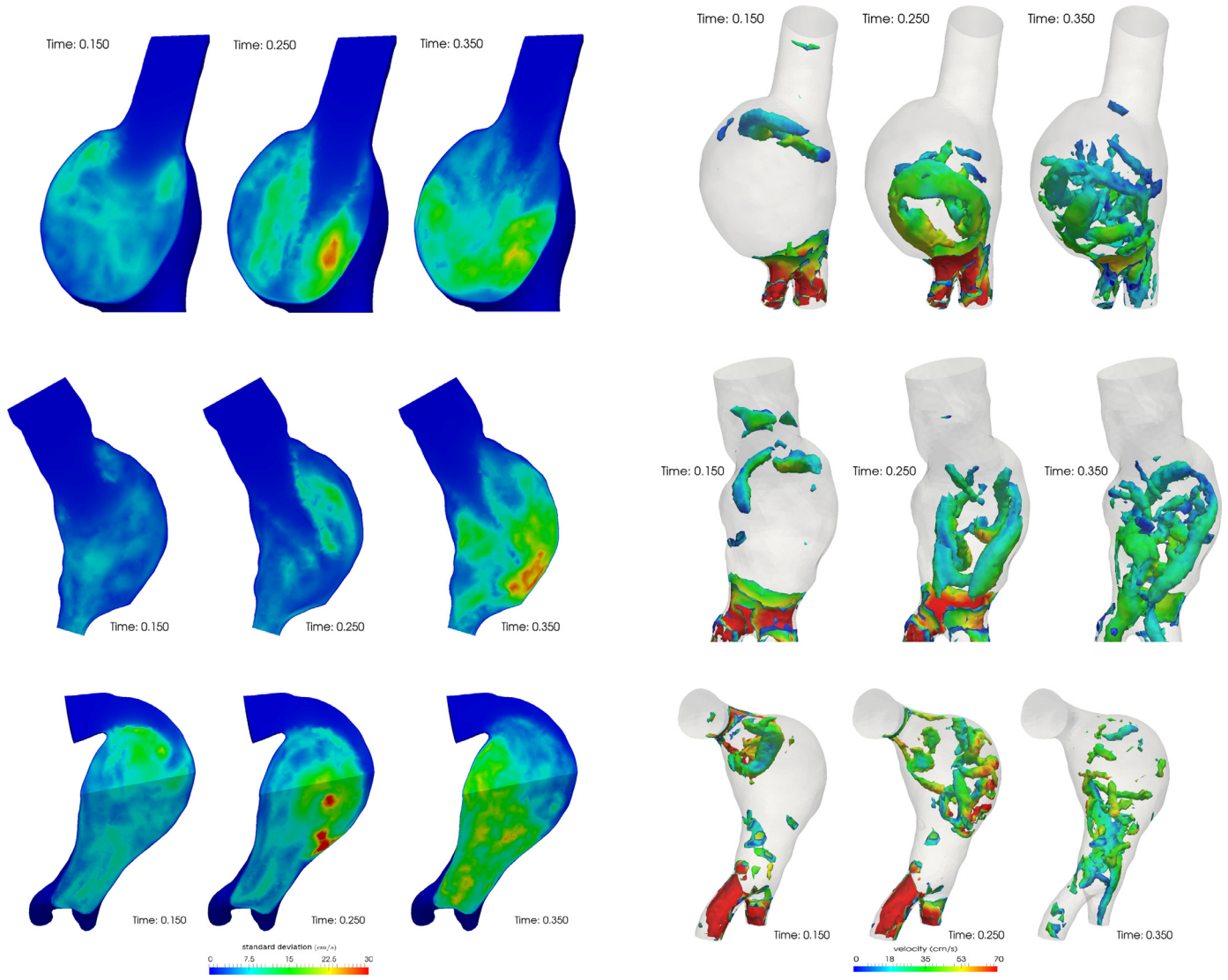

Fig. 4. Left: Standard deviation of the velocity magnitude over 6 heartbeats. Right: Q-criterion (we report the regions with $Q > 5000$ painted by the velocity magnitude). Top: Results for P1; Middle: Results for P2; Bottom: Results for P3. Three time instants are reported for each case: Systolic peak instant $t = 0.15\,s$; Mid-deceleration $t = 0.25\,s$; Early diastole $t = 0.35\,s$.

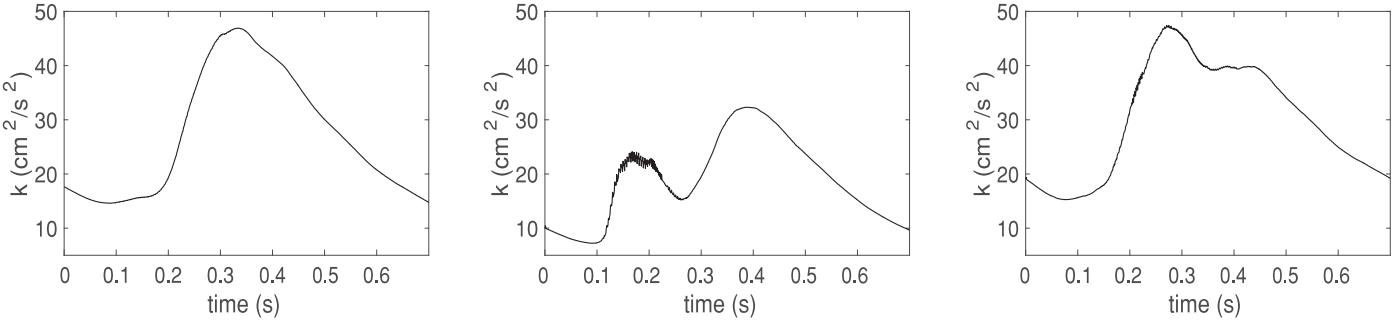

Fig. 5. Global Turbulent Kinetic Energy $k(t)$ over 6 heartbeats for the three patients. Left: P1; Middle: P2; Right: P3.

We observe that, for all cases, the peak value is reached during the mid-deceleration phase ($t \simeq 0.3 - 0.4\,s$). Moreover, we observe significant lower values for P2 with respect to P1 and P3, confirmed also by the mean and maximum in time values reported in Table 1, where we report also the dimensions of the three AAA.

The peak systolic Reynolds number for all the cases is computed as

$$Re = \frac{V_{sist} D}{\nu} = \frac{4 Q_{sist}}{\pi D \nu} \simeq 2200,$$

where V_{sist} is the mean systolic velocity at the inlet, $Q_{sist} = 120\,\mathrm{cm}^3/s$ the systolic flow rate prescribed at the inlet (see Fig. 1), and $D \simeq 2\,\mathrm{cm}$ a representative value, for all the patients, of the diameter at the inlet.

Last, in Fig. 6 we report the spatial distribution of the ensemble-averaged WSS over 6 heartbeats at the time instant where it reaches its maximum value ($t = 0.3\,s$). From this figure, we observe large values in correspondence of the impingement regions.

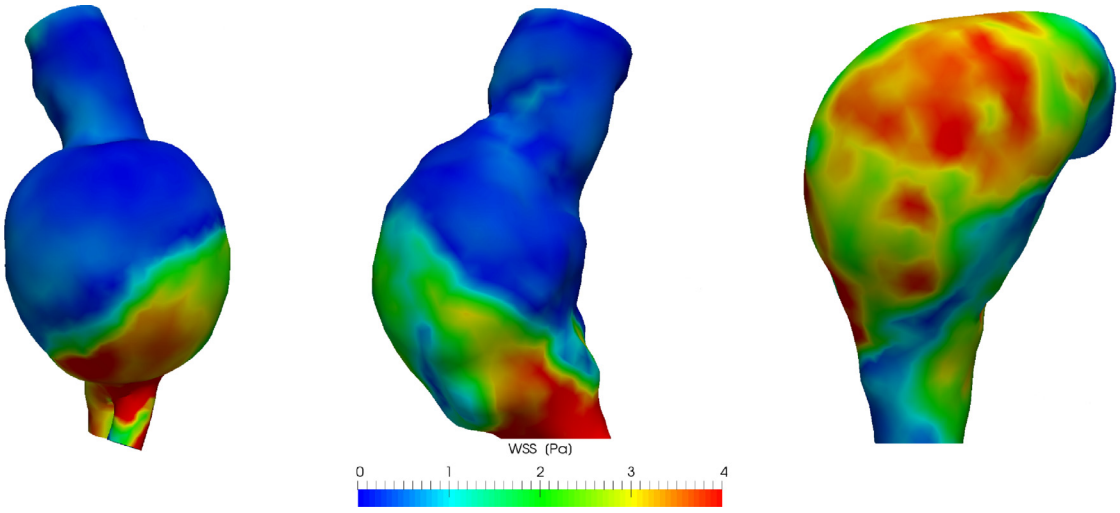

Fig. 6. Peak ensemble-averaged Wall Shear Stress over 6 heartbeats ($t = 0.3\,s$). Left: P1; Middle: P2; Right: P3.

4. Discussion

4.1. The presence of turbulence in abdominal aortic aneurysms and its clinical implications

The presence of turbulence in healthy vascular vessels seems to be confined to the ascending and thoracic aorta. However, these effects are quite negligible since, in physiological conditions, the helicity developed in such districts as a consequence of the ventricular contraction reduces the turbulent kinetic energy [30]. A different situation occurs in pathological districts, where significant transition to turbulence effects could develop, often as a consequence of a change of the geometry. For example, this is the case of stenotic carotids [12–15,31–34].

Turbulence effects in abdominal aortic aneurysms due to the sudden change of geometric shape and to pulsatility have been observed in-vivo by means of the Echo-Color Doppler (ECD) technique [5]. Also in-vitro experiments in idealized AAA have been set up to study the presence of turbulence. In particular, ECD has been used to highlight the presence of turbulence in steady conditions when the Reynolds number (Re) is greater than 2250 [10,35], a laser Doppler velocimeter (LDV) has revealed the presence of turbulence under steady exercise conditions ($Re \simeq 4000$) [6], and similar experiments highlighted that under pulsatility conditions turbulence may occur at lower Re values (peak value $Re \simeq 2300$) [8,36,37].

The presence of turbulence effects in AAA carries a significant clinical impact. In the initial phases of AAA development, turbulence interferes with endothelial cells turnover, which is at the basis of atherosclerosis development, also at relative low level of shear stresses [7]. This is probably due to high-frequency fluctuations, to the rapidly changing direction of shear stress, and to the comparable dimensions of the smallest turbulent eddies and endothelial cells. In the more advanced stages of AAA development, turbulence produces increased wall shear stresses compared with laminar flows, which may be responsible for further aneurysm dilatation, since the abdominal aorta regulates its diameter to maintain the shear stress below a physiological value [38]. Moreover, the increased shear stresses together with aortic wall vibration due to the large fluctuations, could damage the vessel wall, with possible implications on aneurysm growth and rupture [10,39]. Finally, turbulent flows probably damage blood platelets promoting the formation of intraluminal thrombus (ILT) inside the aneurysmatic sac [3,8].

4.2. Overview of computational studies

For all these reasons, some authors included the analysis of turbulence and/or transitional effects in their studies of blood dynamics in AAA. Rigid ideal geometries under steady conditions have been considered [10,40], where the increase of turbulent fluctuations in the distal part of the aneurysm has been reported, whereas the analysis for similar geometries and under pulsatile physiological conditions revealed the presence of vortices detaching from the wall and travelling towards the distal neck [9,36]. The inclusion of the aortic wall deformation in ideal AAA geometries resulting in a fluid-structure interaction analysis has been also considered for the study of turbulence effects [41]. Studies of turbulence effects in realistic AAA geometries reconstructed by radiological images have been carried out, reporting the influence of exercise conditions [11] and highlighting the relationship of such effects with the thrombus formation [3].

Regarding the turbulent models included in these studies, the $k-\varepsilon$ [9] and $k-\omega$ [41] models were also considered, whereas a Direct Numerical Simulation was realized elsewhere [11]. A LES model implemented in a commercial software was also used [42,43]; however no information on the LES model was provided and no analysis of turbulence was reported, the focus of these papers being the influence of boundary conditions and the monocyte deposition, respectively.

One of the major difficulties in computational models relies on a proper definition of suitable quantities capable to describe and quantify the turbulent and transitional effects in AAA. Often, the presence of such effects has been simply related to the formation of vortices and disturbed flow. However, some authors provided more statistically-sound quantities to assess turbulence in AAA. The standard deviation of the velocity field has been computed to assess and localize the presence of velocity fluctuations [10], whereas the Turbulent Kinetic Energy has been reported as a similar quantification of turbulent instabilities [11,41].

4.3. Discussion of the methods

In this study we considered a LES model implemented in the Finite Element library LIFEV. In particular, we used the eddy viscosity $\sigma-$model, which vanishes in the cases of pure rotation, pure shear, or when the resolved scales are in axisymmetric or isotropic expansion. Moreover, the turbulent stresses decay as the distance to the solid boundary to the third power [18]. These features make

the $\sigma-$model suitable to simulate fluids in enclosed domains and in presence of shear layers as in the present case. In principle, the model is well suited to describe cases (like the present one) where both spatial and temporal instabilities are present. For these reasons, it has been successfully applied to describe ventricular blood dynamics [44]. Our implementation of the $\sigma-$ model has been validated elsewhere [24], where a comparison with a DNS solution highlighted the accuracy of this LES model when used in coarse meshes of stenotic carotids.

Blood has been modeled as a constant density, Newtonian, and homogeneous fluid, a well-accepted hypothesis in the previous studies of turbulence effects in AAA [3,11,41]. However, we observe that the Newtonian hypothesis may be considered as a limitation of the present study, since the small eddies arising as a consequence of turbulent or transitional effects may justify the use of a non-Newtonian rheology [9]. We also assumed rigid walls, another well accepted hypothesis in this context [3,9,11], which however represents in fact a second limitation of the present work. Indeed, some differences with respect to the complete fluid-structure interaction (FSI) model have been highlighted [9]. In particular, the rigid wall assumption seems to slightly overestimate the turbulence kinetic energy. Regarding boundary conditions, in absence of measures, we prescribed a representative flow rate at the inlet, whereas zero stresses are set at the iliac outlets. The latter conditions could be justified by noticing that the resistance downstream the two iliac tracts should be equal in physiological conditions. However, the prescription of patient-specific velocity data obtained, for example, by the phase-contrast-MRI technology could provide more accurate results, as highlighted also for AAA [42]. Alternatively, at the outlets boundary conditions based on 3-element windkessel models may be considered for AAA [11]. We also observe that at the inlet we selected a priori a parabolic velocity profile to prescribe the defective flow rate condition (2). This is one the major limitations of the present work. Indeed, this choice could have an impact on the solution if the inlet region is not extended enough to allow the velocity profile to reach a fully developed state. To overcome this drawback, Lagrange multipliers [45,46], optimal control [47], or Nitsche [48,49] approaches could be used to reduce the impact on the solution [50]. Moreover, from radiological dynamic images, it has been observed that blood flow after the thoracic tract is markedly three-dimensional with secondary flows generated by the torsion and curvature of the aorta [51,52].

Despite these drawbacks, in this first study on transitional effects in AAA, we decided to assume a Newtonian rheology and rigid-walls, together with simplified boundary conditions. Since the main focus of the present study is on the suitability of LES models in AAA geometries, we believe that these potential sources of inaccuracy should not influence the general trends and conclusions of the results we are going to discuss in the next section. Of course, we are working to relax them, in order to include FSI, non-Newtonian, and more-realistic boundary conditions in our future studies.

4.4. Analysis of the results

Although many authors speak about turbulence in AAA, here we prefer to refer to instability processes as *transition to turbulence*: the pulsatility of the blood flow on the one hand is responsible for instabilities occurring at lower Reynolds number than in the steady case [8,10], while on the other hand does not allow the complete development of the flow into the turbulent regime. This is prevented by the acceleration phase of a new heartbeat that laminarizes the flow [8].

From our results, we can state that transitional effects are significant in AAA, as confirmed by the large values of the standard deviation of the velocity magnitude (up to 40% of the velocity magnitude itself, see Fig. 4, left). This means that the velocity field presents significant random fluctuations among different heartbeats. By looking at Figs. 2–5 we observe all reported quantities related to the formation of transitional effects (i.e. the ratio between subgrid-scale and molecular viscosities, the standard deviation of the velocity magnitude, the Q-criterion, and the global KTE) being higher during the mid-deceleration phase. This confirms previous observations that at similar Reynolds numbers the flow tends to be very unstable at the beginning of the deceleration [8]. In particular, we find that during the mid-deceleration phase, the flow jet impinges on the aneurysmatic sac creating recirculation regions around the impingement point that propagates proximally around the jet and distally through the iliac outlets. These instabilities are well captured by the distribution of the standard deviation of the velocity magnitude.

Table 1
Values of the craniocaudal length (from the neck to the iliac outlets, in cm), of the antero-posterior and latero-lateral diameters (in cm), and of the mean and maximum in time of $k(t)$ (in cm^2/s^2).

	P1	P2	P3
CC length	4.9	4.9	6.9
AP diameter	4.5	4.1	3.9
LL diameter	4.5	3.9	4.8
k_{mean}	19.0	13.2	21.0
k_{max}	46.8	32.1	47.2

Referring to Figs. 2–4, left, we observe that for all the three patients, the regions with elevated values of the subgrid-scale viscosity are in fact those of disturbed flow (high standard deviation of the velocity magnitude). This confirms the suitability of the $\sigma-$LES model in this context, being able to turn on only where and when needed, with values of the subgrid-scale viscosity reaching up to five times the molecular one. On the other hand, the LES model switches itself essentially off in the laminar regions.

As noticed by observing Fig. 4, right, blood flow is characterized by a vortex ring that originates at the neck of the aneurysm, where a sudden change of diameter occurs. This ring propagates towards the inner region of the aneurysmatic sac and breaks down after the impingement. This phenomenon, at the best of our knowledge observed here for the first time in AAA, seems to be very similar to that taking place in the left ventricle and due to the passage of blood flow through the mitral valve [53,54]. However, some differences are notable. First, the breakage of the vortex ring in AAA is due to the impingement, whereas in the heart it occurs in the middle of the ventricle chamber. This is probably due to the presence in AAA of outlets in the opposite direction of the entrance region. This, unlike the left ventricle featuring no outlets during the diastolic filling, helps the propagation of the ring towards the distal part of the sac. Moreover, as highlighted by the figures on the right ($t = 0.35\,s$), during the diastolic phase the vortex ring transforms into a swirling structure after the impingement. Again, this should be caused by the presence of the iliac outlets that favor the exit of the flow structures.

Analyzing Fig. 5, we observe that the global Turbulent Kinetic Energy is clearly lower for P2 than for P1 and P3. This is also confirmed by the results reported in Table 1, highlighting that both k_{mean} and k_{max} decrease for P2 by more than 30%. By considering these results together with the dimensions of the aneurysms, we observe that P2 is characterized by smaller dimensions of the sac. Possible correlations between the AAA dimensions and the intensity of the global Turbulent Kinetic Energy deserves a particular attention for future studies. We also observe periodic flow instabilities in Patient 2 which are very similar to those observed in cerebral aneurysms [17].

Finally, from Fig. 6 we observe that the higher values of the peak ensemble-averaged WSS are localized at the mid-deceleration phase and in the regions of the impingement, that is where transitional effects occur. These elevated values are due to the impingement itself, but probably they also assume increased value with respect to the laminar case for the presence of transitional effects [9,10,38].

5. Conclusions

In this study, for the first time a large eddy simulation model has been used to study effects related to transition to turbulence in abdominal aortic aneurysms. We found that the considered LES model is capable to turn itself on in regions where the instabilities and fluctuations occur, i.e. around the impingement region at the mid-deceleration phase. Transitional effects were studied by computing the standard deviation of the velocity magnitude and the Q-criterion. The latter quantity highlighted the presence of a vortex ring that starts from the neck of the aneurysmatic sac and propagates within this. After its breakage due to the impingement, this annular structure transforms into a swirling flow that exits through the outlets. Our results also suggested a strong correlation between the dimensions of the AAA and the intensity of the Turbulent Kinetic Energy.

Conflicts of interest

None declared.

Sources of funding for this research

CV and LF have been partially supported by the Italian MIUR PRIN12 project no. 201289A4LX “Modelli matematici e numerici del sistema cardiocircolatorio e loro applicazione in ambito clinico”. CV was also partially supported by INDAM-GNCS. DLV has been supported by the ERC 2015 Proof of Concept “math4AAArisk” (A mathematical platform for Abdominal Aortic Aneurism risk assessment and surgical planning).

Ethical approval

We obtained the Authorisation from the Chief medical Officer of I.R.C.C.S. Fondazione Caâ Granda Policlinico Ospedale Maggiore di Milano - Prot. 2863 04.01.2013.

References

[1] Fleming C, Whitlock E, Beil T, Lederle F. Screening for abdominal aortic aneurysm: a best-evidence systematic review for the U.S. preventive services task force. Ann Intern Med 2005;142(3):203–11.
[2] Bagci E, Vodovotz Y, Billiar T, Ermentrout B, Bahar I. Computational insights on the competing effects of nitric oxide in regulating apoptosis. PLOS One 2008;3(5):e2249.
[3] O'Rourke M, McCullough J, Kelly S. An investigation of the relationship between hemodynamics and thrombus deposition within patient-specific models of abdominal aortic aneurysm. Proc Inst Mech Eng Part H: J Eng Med 2012;226(7):548–64.
[4] Piccinelli M, Vergara C, Antiga L, Forzenigo L, Biondetti P, Domanin M. Impact of hemodynamics on lumen boundary displacements in abdominal aortic aneurysms by means of dynamic computed tomography and computational fluid dynamics. Biomech Model Mechanobiol 2013;12(6):1263–76.
[5] Bluth E, Murphey S, Hollier L, Sullivan M. Color flow doppler in the evaluation of aortic aneurysms. Int Angiol 1990;9(1):8–10.
[6] Egelhoff C, Budwig R, Elger D, Khraishi T, Johansen K. Model studies of the flow in abdominal aortic aneurysms during resting and exercise conditions. J Biomech 1999;32(12):13191329.
[7] Davies P, Remuzzi A, Gordon E, Jr CD, Jr MG. Turbulent fluid shear stress induces vascular endothelial cell turnover in vitro. Proc Natl Acad Sci USA 1986;83(7):2114–17.
[8] Yip T, Yu S. Cyclic transition to turbulence in rigid abdominal aortic aneurysm models. Fluid Dyn Res 2001;29(2):81–113.
[9] Khanafer K, Bull J, Jr GU, Berguer R. Turbulence significantly increases pressure and fluid shear stress in an aortic aneurysm model under resting and exercise flow conditions. Ann Vasc Surg 2007;21(1):67–74.
[10] Asbury C, Ruberti J, Bluth E, Peattie R. Experimental investigation of steady flow in rigid models of abdominal aortic aneurysms. Ann Biomed Eng 1995;23(1):29–39.
[11] Les A, Shadden S, Figueroa C, Park J, Tedesco M, Herfkens R, et al. Quantification of hemodynamics in abdominal aortic aneurysms during rest and exercise using magnetic resonance imaging and computational fluid dynamics. Ann Biomed Eng 2010;38(4):1288–313.
[12] Stroud J, Berger S, Saloner D. Numerical analysis of flow through a severely stenotic carotid artery bifurcation. J Biomech Eng 2002;124(1):9–20.
[13] Grinberg L, Yakhot A, Karniadakis G. Analyzing transient turbulence in a stenosed carotid artery by proper orthogonal decomposition. Ann Biomed Eng 2009;37(11):2200–17.
[14] Lee S, Lee S, Fischer P, Bassiouny H, Loth F. Direct numerical simulation of transitional flow in a stenosed carotid bifurcation. J Biomech 2008;41(11):2551–61.
[15] Rayz V, Berger S, Saloner D. Transitional flows in arterial fluid dynamics. Comput Methods Appl Mech Eng 2007;196(31–32):3043–8.
[16] Yagi T, Sato A, Shinke M, Takahashi S, Tobe Y, Takao H, et al. Experimental insights into flow impingement in cerebral aneurysm by stereoscopic particle image velocimetry: transition from a laminar regime. J Biomech 2013;10(82).
[17] Khan M, Chnafa C, Gallo D, Molinari F, Morbiducci U, Steinman D, et al. On the quantification and visualization of transient periodic instabilities inpulsatile flows. J. Biomech. 2017;52:179–82.
[18] Nicoud F, Toda HB, Cabrit O, Bose S, Lee J. Using singular values to build a subgrid-scale model for large eddy simulations. Phys Fluids 2011;23(8):085106.
[19] Antiga L, Steinman D. Thevascular modeling toolkit (VMTK); 2009. www.vmtk.org.
[20] Quarteroni A, Manzoni A, Vergara C. The cardiovascular system: mathematical modelling, numerical algorithms and clinical applications. Acta Numer 2017;26:365–590.
[21] Rogallo R, Moin P. Numerical simulation of turbulent flows. Ann Rev Fluid Mech 1984;16:99–137.
[22] Smagorinsky J. General circulation experiments with the primitive equations: I. The basic experiment. Mon Weather Rev. 1963;91:99–164.
[23] Pope S. Turbulent flows. Cambridge University Press; 2000.
[24] Lancellotti R, Vergara C, Valdettaro L, Bose S, Quarteroni A. Large eddysimulations for blood dynamics in realistic stenotic carotids. Int J Numer Meth Biomed Eng 2017. doi:10.1002/cnm.2868.
[25] Deardorff J. A numerical study of three-dimensional turbulent channel flow at large Reynolds numbers. J Fluid Mech 1970;41:453–65.
[26] Hairer E, Nørsett S, Wanner G. Solving ordinary differential equations: nonstiff problems. Springer Series in Comput. Math. Springer; 1993. 9783540566700.
[27] Quarteroni A, Valli A. Numerical approximation of partial differential equations. Springer; 1994.
[28] Tezduyar T. Stabilized finite element formulations for incompressible flow computations. Adv Appl Math 1992;28:1–44.
[29] Chong Perry C. A general classification of three-dimensional flow fields. Phys Fluids A 1990;2:765.
[30] Morbiducci U, Ponzini R, Rizzo G, Cadioli M, Esposito A, Montevecchi F, et al. Mechanistic insight into the physiological relevance of helical blood flow in the human aorta: an in vivo study. Biomech Model Mechanobiol 2011;10(3):339–55.
[31] Birchall D, Zaman A, Hacker J, Davies G, Mendelow D. Analysis of haemodynamic disturbance in the atherosclerotic carotid artery using computational fluid dynamics. Eur Radiol 2006;16(5):1074–83.
[32] Tan F, Soloperto G, Bashford S, Wood N, Thom S, Hughes A, et al. Analysis of flow disturbance in a stenosed carotid artery bifurcation using two equation transitional and turbulence models. J Biomech Eng 2008;130(6):061008.
[33] Fischer P, Loth F, Lee S, Lee S, Smith D, Bassiouny H. Simulation of high-Reynolds number vascular flows. Comput Methods Appl Mech Eng 2007;196:3049–60.
[34] Cheung S, Wong KKL, Yeoh GH, Yang W, Tu J, Beare R, et al. Experimental and numerical study on the hemodynamics of stenosed carotid bifurcation. Australas Phys Eng Sci Med 2010;33(4):319–28.
[35] Peattie R, Asbury C, Bluth E, Ruberti J. Steady flow in models of abdominal aortic aneurysms. part i: Investigation of the velocity patterns. J Ultrasound Med 1996;15(10):679–88.
[36] Fukushima T, Matsuzawa T, Homma T. Cyclic transition to turbulence in rigid abdominal aortic aneurysm models. Biorheology 1988;26(2):109–30.
[37] Peattie R, Riehle T, Bluth E. Pulsatile flow in fusiform models of abdominal aortic aneurysms: flow fields, velocity patterns and flow-induced wall stresses. J Biomech Eng 2004;126(4):438–46.
[38] Giddens D, Zarins C, Glagov S. Response of arteries to near-wall fluid dynamic behavior. Appl Mech Rev 1990;43(5S):S98–S102.
[39] Johansen K. Aneurysms. Sci Am 1982;247(1):110–25.
[40] Budwig R, Elger D, Hooper H, Slippy J. Steady flow in abdominal aortic aneurysm models. J Biomech Eng 1993;115:418–23.
[41] Khanafer K, Bull J, Berguer R. Fluid-structure interaction of turbulent pulsatile flow within a flexible wall axisymmetric aortic aneurysm model. Eur J Mech - B/Fluids 2009;28(1):88–102.
[42] Hardman D, Semple S, Richards J, Hoskins P. Comparison of patient-specific inlet boundary conditions in the numerical modelling of blood flow in abdominal aortic aneurysm disease. Int J Numer Meth Biomed Eng 2013;29:165–78.

[43] Hardman D, Doyle B, Semple S, Richards J, Newby D, Easson W, et al. On the prediction of monocyte deposition in abdominal aortic aneurysms using computational fluid dynamics. Proc Inst Mech Eng Part H: J Eng Med 2013;227(10):1114–24.
[44] Chnafa C, Mendez S, Nicoud F. Image-based large-eddy simulation in a realistic left heart. Comput Fluids 2014;94:173–87.
[45] Formaggia L, Gerbeau J, Nobile F, Quarteroni A. Numerical treatment of defective boundary conditions for the Navier-Stokes equation. SIAM J Numer Anal 2002;40(1):376–401.
[46] Veneziani A, Vergara C. Flow rate defective boundary conditions in haemodinamics simulations. Int J Numer Methods Fluids 2005;47:803–16.
[47] Formaggia L, Veneziani A, Vergara C. A new approach to numerical solution of defective boundary value problems in incompressible fluid dynamics. SIAM J Numer Anal 2008;46(6):2769–94.
[48] Zunino P. Numerical approximation of incompressible flows with net flux defective boundary conditions by means of penalty technique. Comput Methods Appl Mech Eng 2009;198(37–40):3026–38.
[49] Vergara C. Nitsche's method for defective boundary value problems in incompressibile fluid-dynamics. J Sci Comp 2011;46(1):100–23.
[50] Formaggia L, Vergara C. Prescription of general defective boundary conditions in fluid-dynamics. Milan J Math 2012;80(2):333–50.
[51] Markl M, Draney M, Miller D, Levin J, Williamson E, Pelc N, et al. Time-resolved three-dimensional magnetic resonance velocity mapping of aortic flow in healthy volunteers and patients after valve-sparing aortic root replacement. J Thorac Cardiovasc Surg 2005;130(2):456–63.
[52] Morbiducci U, Ponzini R, Gallo D, Bignardi C, Rizzo G. Inflow boundary conditions for image-based computational hemodynamics: Impact of idealized versus measured velocity profiles in the human aorta. J Biomech 2013;46(1):102–9.
[53] Seo J, Vedula V, Abraham T, Lardo A, Dawoud F, Luo H, et al. Effect of the mitral valve on diastolic flow patterns. Phys Fluids 2014;26(12):121901.
[54] Mittal R, Seo J, Vedula V, Choi Y, Liu H, Huang H, et al. Computational modeling of cardiac hemodynamics: current status and future outlook. J Comput Phys 2016;305:1065–82.